Coupler Microwave-Activated Controlled-Phase Gate on Fluxonium Qubits

Ilya A. Simakov[1,2,3,*] Grigoriy S. Mazhorin[1,2,3] Ilya N. Moskalenko[2,†] Nikolay N. Abramov,[2]
Alexander A. Grigorev,[2] Dmitry O. Moskalev,[4,5] Anastasiya A. Pishchimova,[4,5] Nikita S. Smirnov,[4,5]
Evgeniy V. Zikiy,[4,5] Ilya A. Rodionov[4,5] and Ilya S. Besedin[1,2,‡]

[1] *Russian Quantum Center, Skolkovo, Moscow 143025, Russia*
[2] *National University of Science and Technology "MISIS", Moscow 119049, Russia*
[3] *Moscow Institute of Physics and Technology, Dolgoprudny 141701, Russia*
[4] *Dukhov Research Institute of Automatics (VNIIA), Moscow 127055, Russia*
[5] *FMN Laboratory, Bauman Moscow State Technical University, Moscow 105005, Russia*

Tunable couplers have recently become one of the most powerful tools for implementing two-qubit gates between superconducting qubits. A tunable coupler typically includes a nonlinear element, such as a superconducting quantum interference device, which is used to tune the resonance frequency of an LC circuit connecting two qubits. Here we propose a complimentary approach where instead of tuning the resonance frequency of the tunable coupler by applying a quasistatic control signal, we excite by microwave the degree of freedom associated with the coupler itself. Because of strong effective longitudinal coupling between the coupler and the qubits, the frequency of this transition strongly depends on the computational state, leading to different phase accumulations in different states. Using this method, we experimentally demonstrate a controlled-Z gate of 44-ns duration on a fluxonium-based quantum processor, obtaining a fidelity of 97.6% $\pm$ 0.4% characterized by cross-entropy benchmarking.

I. INTRODUCTION

During the last decade, there has been tremendous progress in implementing fluxonium qubits [1–4] as the building blocks of a superconducting quantum processor. Since their proposal [1], fluxoniums have become a perspective experimental platform for creating superconducting quantum circuits with a wide range of control parameters due to their richer energy level structure compared to widely used transmons [5,6]. Because of its large anharmonicity, the fluxonium qubit has significant advantages over the transmon qubit in terms of coherence times, single-qubit gate fidelities, and leakage rates. Fluxonium circuits implemented in a two-dimensional (2D)

_____

*simakov.ia@phystech.edu
†Present address: Department of Applied Physics, Aalto University, Espoo, Finland
‡Present address: Department of Physics, ETH Zurich, Zurich, Switzerland

architecture [3] showed qubit coherence of times T_1, $T_{2e} \approx$ 300 μs, while fluxonium qubits installed in 3D cavities demonstrated coherence times higher than 1 ms and average single-qubit gate fidelities above 0.9999 [7].

The implementation of two-qubit gates on the fluxonium platform has moved from directly coupled qubits [8,9] to a more scalable approach with tunable interaction via a coupler element [10]. Similar to transmons, two-qubit gates on fluxoniums can be implemented using the flux tunability of qubits. The obvious disadvantage of tuning the flux is that the coherence time of the qubit is only large when operated at the flux sweet spot. Another disadvantage of flux-activated gates is that sweeping the frequency of the qubits leads to a Landau-Zener-type interaction with strongly coupled two-level defects that would normally be off-resonant with the qubit [11]. This has been identified as a major problem when many two-qubit gates need to be performed [12,13].

An alternative way of implementing two-qubit gates is by inducing transition interactions between the qubits with microwaves. Microwave-activated gates include transitions via higher-excited energy levels [8,14] or cross-resonance gates [15,16]. These gates rely on direct capacitive coupling between the qubits, which has a drawback of large residual ZZ interactions between the qubits when no gate is applied.

In this paper, we propose a controlled-Z (CZ) gate scheme between two low-frequency fluxoniums coupled via an extra coupler fluxonium. Instead of applying a magnetic flux to the coupler element to change the coupling strength between the qubits, we activate microwave transitions in the coupler element. Because of a strong interaction between this element and the computational qubits, the spectrum of these transitions is state dependent. As a result, the detuning of the microwave drive depends on computational states, which results in different acquired phases in these states. This gate principle is closely related to the microwave-activated CZ gate [8], as well as the *i*-Toffoli gate proposal [17]. Compared to the former, we obtain the geometric phase by exciting a tunable coupler element's degree of freedom, which allows us to lower the residual coupling to below 10 kHz. Compared to the latter, we do not consider a three-qubit gate, where the qubit directly coupled to two neighbors is driven, but rather relabel the driven qubit as the coupler. This allows us to ignore the residual coupling between the driven element and the computational qubits, since the coupler is de-excited when no gate is being performed, significantly simplifying the circuit. We experimentally demonstrate the coupler microwave-activated controlled phase (CMACP) by tuning up a 44-ns-long CZ gate with a cross-entropy benchmarking fidelity of 97.6% $\pm$ 0.4%.

II. DEVICE AND THEORETICAL BACKGROUND

We investigate a quantum device consisting of three capacitively coupled fluxonium qubits, two of which are the computational qubits and the remaining one plays the role of a tunable coupler; see Fig. 1(a). Each fluxonium

has an additional harmonic mode with a frequency close to 2 GHz. The mutual capacitances between the qubits lead to large transversal couplings between the bare fluxonium and harmonic modes. The details of the circuit layout and parameters are discussed in detail in Refs. [10,18].

Here, the computational qubits are biased at their flux degeneracy points, and the coupler is at zero flux. At the operating point the frequencies of the computational qubits are 669.6 and 694.4 MHz, while the coupler frequency is about 3.4 GHz. At these flux biases, when the coupler is de-excited, the residual effective ZZ and XX couplings between the computational qubits are weak, -10 and 500 kHz, respectively.

We consider the ground and excited states of each fluxonium mode, and a microwave signal applied to the coupler close to its resonance frequency. With all fluxoniums being detuned from each other, the transversal couplings result in state dressing and dispersive frequency shifts. The hybridization of the first coupler state with the higher fluxoniums' levels result in the dispersive frequency shifts of the main coupler transition. The shifts for the first and second qubits are respectively equal to 30 and 26 MHz. We schematically show the interaction and the resulting dispersive shift of the coupler 0-1 transition in Fig. 1(b). Because of the very large frequency difference between the coupler and the qubits we neglect driving of the dressed computational qubit modes. Thus, the effective Hamiltonian of the coupled multifluxonium system can be expressed as

$$\frac{\mathcal{H}}{\hbar} = -\sum_{i=1,2,c} \frac{\omega_i}{2}\sigma_{zi} - \sum_{i=1,2} \frac{\zeta_{ic}}{4}\sigma_{zi}\sigma_{zc} + \Omega\sigma_{xc}\cos\omega_d t, \quad (1)$$
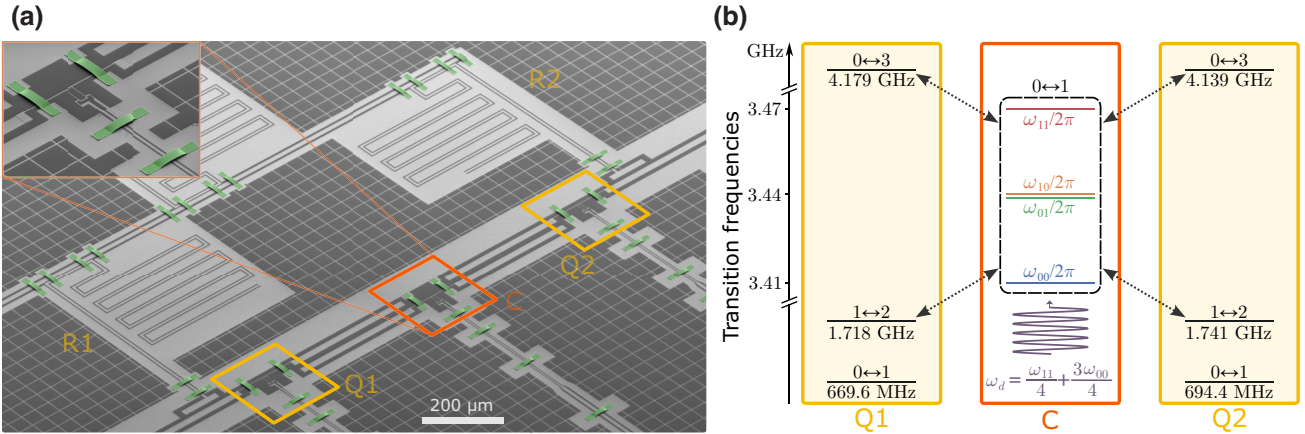

FIG. 1. The device and gate concept. (a) The SEM image of the fluxonuim quantum processor. The computational qubits Q1 and Q2 are capacitively coupled to the individual readout resonators R1 and R2, those in turn are connected to the readout transmission line. Both qubits are also capacitively coupled to the middle fluxonium C, an enlarged image of which is shown in the upper left corner. Each fluxonium has its own excitation line. (b) Schematic diagram of the relevant fluxonium state transitions. The arrows show the interaction between the higher fluxoniums' energy transitions and the coupler 0-1 transition that results in the dispersive shift of the coupler. The frequencies ω_{ij} correspond to the coupler 0-1 transitions, associated with the $|ij\rangle$ state of the computational qubits. With the violet color we depicted the external microwave drive on the coupler required for the proposed gate implementation.
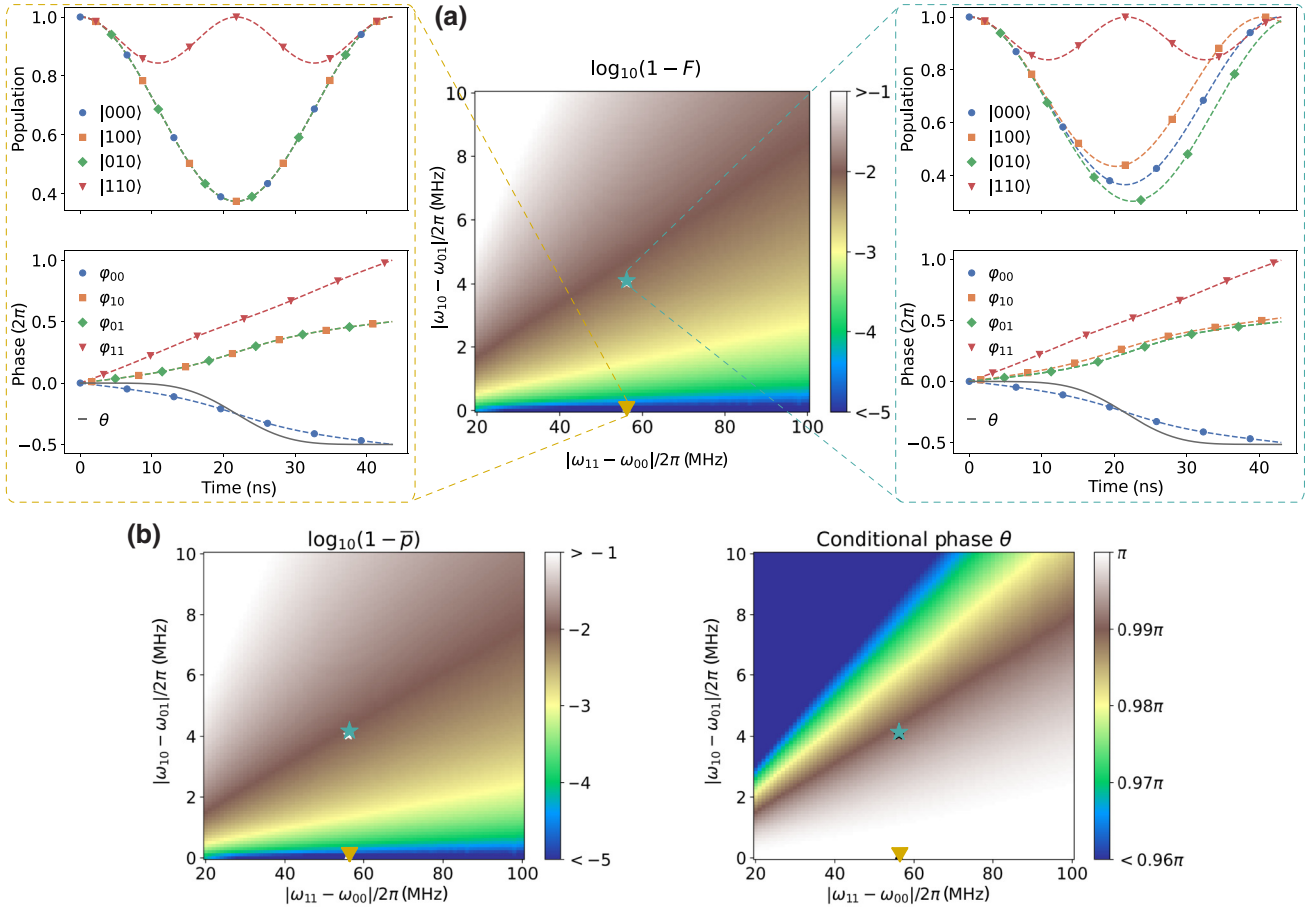
FIG. 2. Gate simulation. (a) The fidelity of a CZ gate $\log_{10}(1-F)$ as a function of the differences between the design-dependent transition frequencies ω_{10}, ω_{01} and ω_{11}, ω_{00}. The orange triangle corresponds to the ideal point when $\omega_{10} = \omega_{01}$ and the left inset plots show the time evolution of the population and common phase of the four computational states. The dashed gray line shows the acquired phase $\theta = \varphi_{00} - \varphi_{10} - \varphi_{01} + \varphi_{11}$. The fidelity of such a gate is exactly 1. The turquoise star corresponds to the frequencies observed in the experiment (see Table I below). The time dynamics of the computational states associated with the ground state of the coupler and the common phases are shown in the right inset figures. The obtained CZ gate fidelity is 0.992. (b) The average population $\log_{10}(1-\overline{p})$ and the accumulated phase θ of a CZ gate as a function of the differences between the transition frequencies. We mention that the conditional phase in the blue area reaches a value of 0.5π.

where $\omega_i/2\pi$ is the renormalized frequency of the ith qubit, ζ_{ic} is the dispersive coupling strength between the computational qubits and the coupler, σ_{xi} and σ_{zi} are Pauli operators acting on the lowest two levels of the ith fluxonium, and Ω is the drive strength. Here we also neglect the direct interaction between the computational qubits since $\zeta_{12} \ll \zeta_{1c}, \zeta_{2c}$.

The Hilbert space of the system can be separated into four noninteracting subspaces corresponding to different states of the computational qubits. We focus on the transitions between the ground and excited states of the coupler in these subsystems. Within a rotating-wave approximation in the frame of the drive signal, their Hamiltonians can be written as

$$\frac{\mathcal{H}}{\hbar} = -\frac{\Delta_{mn}}{2}\sigma_{zc} + \frac{\Omega}{2}\sigma_{xc}, \quad (2)$$

where $\Delta_{mn} = \omega_d - \omega_{mn}$ is the detuning between the drive tone and the effective coupler frequency corresponding to the computational state $mn \in \{|00\rangle, |01\rangle, |10\rangle, |11\rangle\}$,

$$\omega_{mn} = \omega_c + \frac{(-1)^m}{2}\zeta_{1c} + \frac{(-1)^n}{2}\zeta_{2c}. \quad (3)$$

The energy spectrum of the coupler is schematically shown in Fig. 1(b).

The solution of the Schrödinger equation in the case of a rectangular microwave pulse with the ground-state initial condition on the wave function $\psi(0) = |0\rangle$ is

$$\psi(t) = \begin{pmatrix} (i\Delta_{mn}/\Omega_R)\sin(\Omega_R t/2) + \cos(\Omega_R t/2) \\ -(i\Omega/\Omega_R)\sin(\Omega_R t/2) \end{pmatrix}, \quad (4)$$

TABLE I. Measured transition frequencies between the ground and excited states of the coupler for the four logical states of the computational qubits, $|00\rangle$, $|01\rangle$, $|10\rangle$, and $|11\rangle$, with corresponding frequencies ω_{00}, ω_{01}, ω_{10}, and ω_{11}. The errors are calculated as a standard deviation of the least-squares method.

	$\omega_{00}/2\pi$	$\omega_{10}/2\pi$	$\omega_{01}/2\pi$	$\omega_{11}/2\pi$	
Value	3.4098	3.440 09	3.436 05	3.4660	GHz
σ	0.1	0.07	0.08	0.2	MHz

where $\Omega_R = \sqrt{\Delta_{mn}^2 + \Omega^2}$ is the generalized Rabi frequency. Apart from the population transfer, these oscillations also result in a phase accumulation of the computational state. Note that, for an integer number of Rabi oscillations, this phase is either π or 2π.

Thereby, each subspace has its own common phase, which depends on the signal detuning from the frequency of the corresponding transition. The idea is to find such parameters of the drive pulse that the coupler returns to the ground state for all computational states and the common phases φ_{mn} acquired by the Rabi oscillations of the corresponding transition satisfy the condition

$$\theta = \varphi_{00} - \varphi_{10} - \varphi_{01} + \varphi_{11} = \pi + 2\pi k, \qquad k \in \mathbb{Z}. \quad (5)$$

Let us make an assumption that the transitional frequencies ω_{10}, ω_{01} are equal: $\omega_{10} = \omega_{01} = (\omega_{11} + \omega_{00})/2$. In this case both conditions mentioned above can be exactly satisfied, and a CZ gate can be implemented if we choose the drive frequency ω_d at the half sum of the transition ω_{00} and ω_{10}: $\omega_d = (\omega_{10} + \omega_{00})/2$, the amplitude $\Omega = \sqrt{5/12}(\omega_{10} - \omega_{00})$, and the duration $\tau = \sqrt{6}\pi/(\omega_{10} - \omega_{00})$. Such a signal results in a single Rabi oscillation for the $|00\rangle$, $|01\rangle$, and $|10\rangle$ computational states, and two oscillations for the $|11\rangle$ state. The time dynamics of these four populations and the corresponding common phases under the described external signal are shown in the left inset figures of Fig. 2. We calculate the evolution in the rotating-wave approximation assuming that the oscillations are independent and isolated from the rest system.

Though the qubits are designed to be identical, the critical currents of the phase slip junctions turn out slightly different; thus, the transition frequencies ω_{10} and ω_{01} are not equal. We simulate the evolution of the system for the different $|\omega_{11} - \omega_{00}|$ and $|\omega_{10} - \omega_{01}|$ under the drive with frequency $\omega_d = (\omega_{11} + 3\omega_{00})/4$, amplitude $\Omega = \sqrt{5}(\omega_{11} - \omega_{00})/4\sqrt{3}$, and duration $\tau = 2\sqrt{6}\pi/(\omega_{11} - \omega_{00})$. The average population over the four initial states, accumulated conditional phase θ, and fidelity of the obtained CZ gate fidelity calculated on the computational states $|000\rangle$, $|100\rangle$, $|010\rangle$, $|110\rangle$ are shown in Fig. 2. The turquoise star in the plot indicates the point corresponding to the obtained experimental data (see Table I below); the time dynamics of the four populations and the acquired phase for these

frequencies is also shown in the right inset plots of Fig. 2. The fidelity of the simulated gate for the experimental frequencies is 0.992 and the duration is 43 ns.

Besides, we mention yet another possible method to realize a CZ gate via the first excited state of the coupler. If one drives the coupler fluxonium directly at the frequency of the $|110\rangle$-$|111\rangle$ transition for the duration of a single Rabi oscillation, that state acquires a phase of π. If the amplitude of the drive signal is low compared to the frequency detuning $\omega_{11} - \omega_{10}$ then one can ignore the oscillations between the levels $|000\rangle$-$|001\rangle$, $|100\rangle$-$|101\rangle$, and $|010\rangle$-$|011\rangle$ and get a CZ gate with a given accuracy. Unfortunately, the duration of this drive for a high-fidelity gate is several times longer than for the previous method. We provide the numerical estimates in Appendix A. Below focus on the faster detuned-drive CZ gate implementation.

III. EXPERIMENTAL RESULTS

The setup used in this experiment is based on an earlier work [10], with a number of modifications, described in Appendix B. The device characteristics are provided in Appendix C. Here we just briefly summarize the techniques used for single-qubit gates, readout, and initialization, and then focus on the coupler microwave-activated CZ gate implementation.

The reset procedure is realized via capacitively coupled microwave antennas as dissipation channels. We tune the qubit to the zero flux point, where the longitudinal relaxation rate is an order of magnitude higher, and then return the qubit to the operating point just before the scheduled pulse sequence. The readout is implemented using adjacent resonators with fidelities 0.67 and 0.62 for the first and second computational qubits for simultaneous qubit measurement. We explain such a poor readout fidelity by weak coupling strength between the qubit and corresponding resonator, which is an innate feature of the chip layout. The single-qubit gates are generated from $\pi/2$ rotations around axes in the equatorial plane of the Bloch sphere, realized by Gaussian pulses with 13.3-ns duration. The excitation pulses are applied through to the flux line of the qubit. Because of the large amplitudes of these pulses we apply a phase error compensation with a virtual rotation about the Z axis after every $\pi/2$ pulse. We construct each of the 24 elements of the single-qubit Clifford group from two $\pi/2$ gates and virtual Z rotations (see Appendix D). The average fidelity of single-qubit Clifford group gates, $F = 0.9928 \pm 0.0003$, has been measured with the cross-entropy benchmarking method (see Fig. 6 below).

Going back to the CZ gate realization, first, we should note that our device contains no resonator intended for the readout of the coupling fluxonium, and therefore we cannot measure the coupler directly. To deal with this problem, we use the coupler state-dependent frequency shift of the

computational qubits. Before reading out one of the computational qubits, we apply a low-amplitude, 120 ns-long π pulse. The frequency of this pulse corresponds to the qubit frequency when the coupler is unexcited. If the coupler is excited, such an excitation pulse will be out of resonance with the qubit, only weakly affecting the qubit state (see Appendix E for details).

The calibration procedure of the CZ gate starts with determining the transition frequencies of the coupler for the four different states of the computational qubits. For this, we perform the pulse sequence shown in Fig. 3(a). We prepare the computational qubits in one of the four initial states $|00\rangle$, $|10\rangle$, $|01\rangle$, $|11\rangle$ and then apply a microwave pulse on the coupler, varying the frequency and duration. After that, the coupler state measurement protocol consisting of a low-amplitude X gate applied to one of the qubits followed by the measurement of that qubit is performed. In this manner, we observe Rabi chevron patterns, from which we extract Rabi frequencies for each detuning of the drive signal. We approximate the data by the formula $\sqrt{\Omega^2 + \Delta_{mn}^2}$, where the drive amplitude Ω and the resonance Rabi frequency ω_{mn} are the fitting parameters. We collect the results in Table I and plot the drive dependence of the Rabi frequency in Fig. 3.

Using the obtained transition frequencies, we calculate the gate duration for an optimal rectangular pulse and experimentally find the corresponding amplitude. Thus we roughly define the frequency, amplitude, and duration of the drive pulse. For the precise calibration, we execute the gate sequence shown in Fig. 4, which is commonly used for the phase estimation of a controlled-phase (CPHASE) gate [19]. In this experiment we measure the population of the second qubit as a function of the phase φ of the highlighted gate when the first qubit is initially in the $|0\rangle$ and $|1\rangle$ states. These populations are fitted with the functions

$$p_I(\varphi) = \tfrac{1}{2}(1 - \cos(\varphi + \varphi_2)),$$
$$p_X(\varphi) = \tfrac{1}{2}(1 - \cos(\varphi + \varphi_2 + \theta)), \tag{6}$$

and the phase difference θ is the parameter of the CPHASE gate. We measure this angle for different signal amplitudes, fit the obtained points with a line, and find an amplitude corresponding to the π phase; see Fig. 4. Then we measure the period of the Rabi oscillations of the coupler at this amplitude for the computational qubit states $|00\rangle$, $10\rangle$, and $|01\rangle$ (the oscillations associated with state $|11\rangle$ are indistinct under the current experimental conditions), find the best drive frequency, when these states have close Rabi frequencies, and update the gate duration. After that we again refine the amplitude with the previous method. We repeat the procedure 3 times, until the amplitude converges.

Finally, after we determine the parameters of the drive signal, we test the CZ gate. First, we perform a tomography experiment of the two-qubit identity gate I with zero
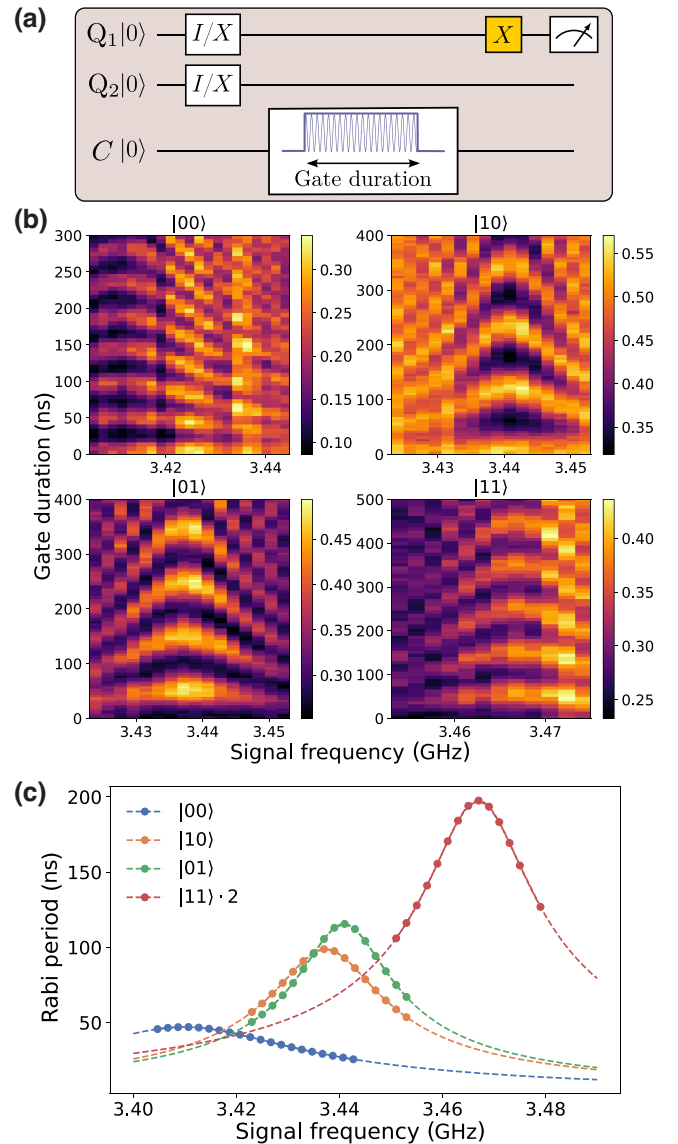

FIG. 3. Rabi oscillations of the coupler for different computational states. (a) The excitation pulse sequence. The first two single-qubit gates set the computational qubits into one of four computational states. Then we apply the rectangular pulse on the coupling qubit of given duration and finally execute an X gate on the first qubit. We highlight the gate as it is calibrated with the coupler at the ground state. Because of these changes we observe Rabi patterns of the coupler via the computational qubit, shown in (b) for the different initial states. (c) The period of coupler Rabi oscillations as a function of the signal frequency obtained from the Rabi patterns. The legend notation $|11\rangle \cdot 2$ means that the period of coupler population oscillations is multiplied by a factor of 2, as, for the CZ gate, two Rabi oscillations of this state are required.

duration, and of the CMACP-generated CZ gate, repeated once and twice. The obtained fidelities are 0.9824, 0.9892, and 0.9637 for the I, CZ, and CZ^2 gates, respectively, and the Pauli process matrices are shown in Fig. 5. The disadvantage of the tomography method is that the result is
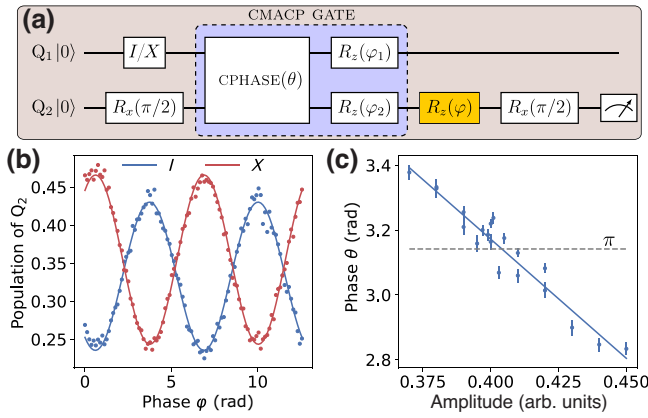
FIG. 4. Calibration of the CZ gate. (a) Excitation pulse sequence. The first qubit is prepared in one of the two states $|0\rangle$ (I gate) or $|1\rangle$ (X gate). Then we apply the coupler microwave-activated controlled-phase gate, make a single-qubit phase rotation on the second qubit, and finally measure the second qubit in the X basis. (b) Populations p_I and p_X of the second qubit as a function of the phase φ of the highlighted gate. The solid lines are fits of the experimental dots with the functions in Eq. (6). (c) Conditional phase θ as a function of the excitation pulse amplitude.

strongly affected by state preparation and measurement (SPAM) errors. Thus, in consideration of the poor readout, the fidelity of the CZ gate turned out to be higher than that of the identity gate. The large difference between the fidelities of the CZ and CZ^2 gates indicates significant residual population of the coupler after the first CMACP gate, expected for the current system parameters. Indeed, if the coupler does not completely return to the ground state after the gate execution, it does not decrease fidelity of the current gate, but has a strong effect on subsequent gates.

Second, we test the CZ gate using the cross-entropy benchmarking technique (XEB) [12,20]. This method accommodates SPAM errors, and is highly sensitive to the
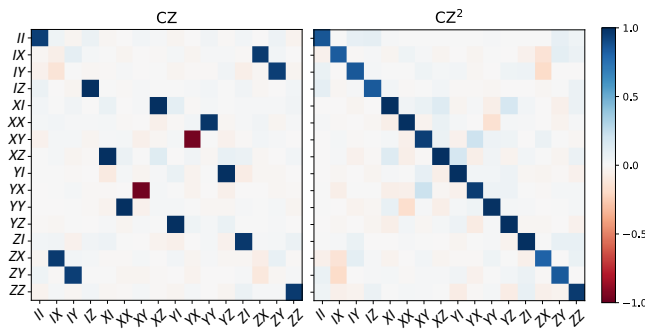

FIG. 5. Experimental reconstruction of the Pauli process matrices for the obtained coupler microwave-activated CZ gate with $F = 0.9892$ and two CZ gates implemented in a row with $F = 0.9637$. For comparison, the fidelity of the identity matrix is $F = 0.9824$.

residual population of the noncomputational states. For the experiment, we test quantum circuits with depth m up to 100; for each depth, we generate 150 sets of two random sequences $\{C_{11}, \ldots, C_{1m}\}$, $\{C_{21}, \ldots, C_{2m}\}$ of the single-qubit Clifford gates and average the readout results over 10 000 repetitions of each of these sets with and without (reference) the interleaved target CZ gate. We approximate the average depolarization fidelity F_{dep} by the function ap^m, where p is the depolarization fidelity per cycle and a is a fitting parameter. The conventional gate fidelity can be calculated with the formula

$$F = p + (1 - p)/D, \tag{7}$$

where $D = 2^n$ is the dimension of the Hilbert space ($n = 2$). If a target gate is inserted after each single-qubit operation then the average fidelity of the gate is determined by Eq. (7) with $p = p_2/p_1$, where p_2 and p_1 are the depolarization fidelities per cycle corresponding to the interleaved and reference sequences [21].

In Fig. 6, blue dots show an exponential decay of the depolarization fidelity of the reference random single-qubit Clifford-gate sequence executed simultaneously on
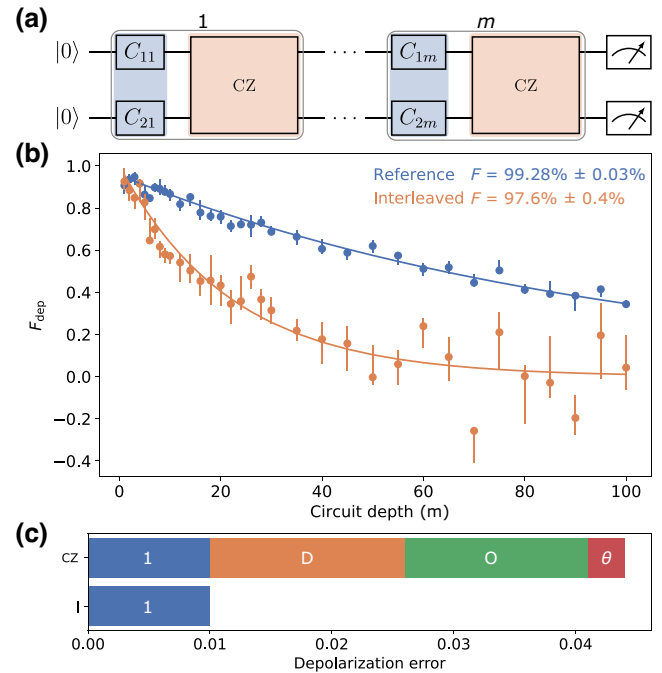

FIG. 6. Cross-entropy benchmarking. (a) Quantum circuit for the XEB experiment. (b) Depolarization fidelity for the XEB sequences without (reference) and with the interleaved target CZ gate. (c) Depolarization error rate estimates for the implemented gate: ε_θ relates to the nonexact π phase of the CZ gate; ε_1 and ε_D correspond to decoherence on the computational qubits during single-qubit and two-qubit gates, respectively; ε_O is the residual error rate that includes effects of the residual population and decoherence of the coupling element.

two computational qubits. The orange dots present similar data with the inserted target CZ gate. With a least-squares fit we obtain $p_1 = 99.00\% \pm 0.05\%$ and $p_2 = 95.6\% \pm 0.4\%$. The average fidelities of the single-qubit Clifford gates and the CMACP-generated CZ gate are $F = 99.28\% \pm 0.03\%$ and $F = 97.6\% \pm 0.4\%$, respectively.

Furthermore, we estimate the contributions of the various error sources to the total error $\varepsilon = 1 - p$ of the CZ gate. The first one is the nonexact conditional phase π. We find that the fidelity of the XEB data is maximized for the phase of the target gate $\theta = 0.963\pi$ and calculate the depolarization infidelity $\varepsilon_\theta = 0.003$. The next error source is decoherence of the computational qubits. This contribution can be estimated by the extrapolation of the average single-qubit error $\varepsilon_1 = 1 - p_1 = 0.01$ from the duration of a single-qubit operation, 26.6 ns, to the CZ gate duration, 44 ns, yielding $\varepsilon_D = 0.016$. The rest infidelity $\varepsilon_O = 0.015$ we attribute to other error sources that include the decoherence processes and residual population on the coupling fluxonium. The estimated error budget is shown with a bar plot in Fig. 6. The coherence rates and numerical estimations are provided in Appendix E. Note that the errors for the interleaved sequences are significantly larger than for the reference sequences. This is related to the larger spread of fidelities for different random sequences, which indicates a significant fraction of coherent errors in the implemented two-qubit gates.

IV. CONCLUSION AND OUTLOOK

In this work, we propose and demonstrate a CZ gate realized using a microwave drive applied to a coupler qubit. Because of the strong interaction between the coupling and computational qubits, the main transition frequency of the coupler depends on the state of the computational qubits. This allows us to choose such exciting pulse that the speed of phase acquisition on the computational states is different, which in turn results in an effective CPHASE operation. We experimentally demonstrate the proposed CZ gate of 0.976 fidelity and 44-ns duration on a device consisting of three capacitively coupled fluxoniums.

The obtained gate fidelity can be improved in further experiments. We identify two significant error sources: decoherence processes and the residual population of the coupler. While decoherence is a significant limiting factor for the performance of many contemporary qubits, the residual population of a degree of freedom mediating the two-qubit interaction is not typical for superconducting qubits. We stress that the latter error has a coherent nature, and can thus be reduced by using advanced control signal shaping [22].

Both the fluxonium-based topology and the two-qubit gate concept considered in our work demonstrate a promising path forward for scalable and fault-tolerant quantum processors with new qubit types. Tunable couplers in multiqubit setups not only help to obtain high-fidelity two-qubit operations but to suppress residual XX- and ZZ-coupling rates and avoid frequency collision [10]. We also emphasize the low frequency of fluxoniums as a way to simplify individual qubit control via using subgigahertz wiring and electronics for gate operations.

APPENDIX A: CZ OPERATION VIA THE $|110\rangle$-$|111\rangle$ TRANSITION

Yet another approach to implement a CZ gate and satisfy condition (5) is a direct 2π-pulse drive on the coupling element nearby the resonance $|110\rangle$-$|111\rangle$ (or $|000\rangle$-$|001\rangle$). The idea of the gate is similar to the general parametric CZ operation, implemented via transition between the $|11\rangle$-$|20\rangle$ states of the computational qubits [8]. Here, we use the first coupler excited state as an auxiliary energy level out of the computational subspace to acquire conditional phase. The major difficulty of the current method is that the signal should not disturb the three transitions $|000\rangle$-$|001\rangle$, $|100\rangle$-$|101\rangle$, and $|010\rangle$-$|011\rangle$; thus, we choose the
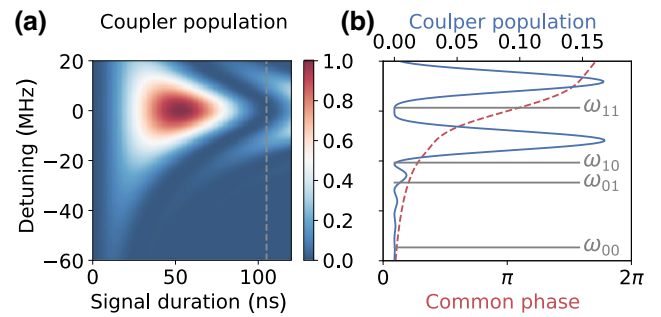

FIG. 7. (a) Rabi oscillations of the coupler population as a function of the exciting pulse frequency and duration. (b) The detuning dependence of the coupler population and the accumulated phase after the first Rabi oscillation, which is shown in the left plot with the gray dashed line. The horizontal lines denote the coupler 0-1 transition associated with the four computational states. Plot (b) illustrates that the gate requires two conditions: the coupler population should return to the ground state and the accumulated phase of the computational states should satisfy condition (5).

Gaussian envelope for the drive of duration τ:

$$\Omega(t) = A \left\{ \exp\left(\frac{(t - \tau/2)^2}{2\sigma^2}\right) - \exp\left(\frac{(\tau/2)^2}{2\sigma^2}\right) \right\} \quad (A1)$$

with A an amplitude and the pulse length truncated by $\sigma = 0.4\tau$. The Rabi pattern caused by this pulse is shown in Fig. 7(a).

Again, to obtain the CZ operation two conditions have to be satisfied simultaneously. First, at the end of the interaction, the coupler should completely return to the initial state. As is illustrated in Fig. 7(b), the amplitude of the gate should be picked up in a way such that the coupler population after the gate is low for all possible effective coupler frequencies. Here, we search for a trade-off between the gate duration and the residual coupler population magnitude. Thus, the amplitude should be low enough that the signal does not disturb the transition associated with the $|01\rangle$ and $|10\rangle$ computational states, and at the same time high enough to cause a fast Rabi oscillation. Second, as can be seen in Fig. 7(b), one cannot neglect the common phase of the computational states $|00\rangle$, $|10\rangle$, and $|01\rangle$ even if the coupler population associated with them is practically unexcited. Since the common phase changes more abruptly at the resonance drive than away from it, this condition can be satisfied if one slightly detunes the signal frequency from ω_{11}.

We simulate the time dynamics of the gate by the Schrödinger equation and obtain the gate of 104-ns duration of fidelity 99.9%. The drive frequency is 3.461 GHz and the resonance $|110\rangle$-$|111\rangle$ frequency is 3.466 GHz. The difference is due to condition (5) and the detuning dependence of the common phase illustrated in Fig. 7(b). This approach has an advantage: it is insensitive to the difference between ω_{01} and ω_{10}. However, it is significantly longer than the method used in the main text; hence, it does not give benefits for systems with poor coherence times.

Varying the detuning of the drive signal one can get not only π, but an arbitrary phase in Eq. (5) and, consequently, obtain a general CPHASE gate with arbitrary phase.

APPENDIX B: EXPERIMENTAL SETUP

The scheme of the experimental setup is presented in Fig. 8. The experiments are performed in a BlueFors LD-250 dilution refrigerator with a base temperature of 10 mK. The chip is connected to the control setup with six lines: the readout line, two excitation and flux control lines (*XYZ* controls), two lines coupled with a 10-mK stage and ended with 50-Ω terminators for qubit reset, and the coupler's excitation and flux control line (*XYZ* controls).

Pulse generation and flux control are fully performed by a Zurich Instruments HDAWG8 arbitrary waveform generator. One analog output port of the generator is used per fluxonium circuit. IQ microwave mixers are employed to up- and down-convert the intermediate frequency readout pulses to the resonator frequencies and back. After getting reflected from the qubit chip, the readout microwave signal is measured by a vector network analyzer (R&S ZVB20) for spectroscopy and a home-built digitizer setup for single-shot readout. For mixer calibration, we use a spectrum analyzer (Agilent N9030A).

Microwave attenuators are used to isolate the qubit chip from thermal and instrumental noise from the signal sources, which are located at room temperature. The readout line is equipped with an impedance matched parametric amplifier (IMPA) followed by a Quinstar CWJ1019KS414 isolator to prevent noise from higher temperature stages entering the IMPA and the qubit device. We pump the IMPA using an Agilent E8257D signal generator. Three Raditec RADC-4.0-8.0-Cryo circulators and a set of low-pass and high-pass filters placed after the sample preserves it from IMPA pumping and reflected signal. At the PT2 stage (3 K) of the cryostat, an LNF-LNC0.3 14A high electron mobility transistor (HEMT) is installed. The output line is further amplified outside the cryostat with two Mini-Circuits ZVA-183-S+ amplifiers. We use a low-pass filter (Mini Circuits VLF-630+) in combination with a powder filter with 15-dB attenuation close to the qubit frequencies in qubit control lines and only a powder filter in the coupler control line.

Capacitively coupled qubit control lines are connected to 50-Ω terminators at the 10-mK stage of the cryostat. These lines are used for the qubit initialization and reset.

APPENDIX C: DEVICE PARAMETERS

The current experimental device and a two-qubit processor described in Ref. [10] are based on a similar design and have been fabricated in the same manufacturing cycles. Using the data obtained during the other sample analysis, we get the qubits and coupler E_C and E_L values. With these two parameters fixed, we find the phase-slip Josephson-junction energy from the frequency at the sweet spot. The device parameters are given in Table II. Also, we provide fundamental transition frequencies f_{01} of each element and coherence times, measured by the standard decay and Ramsey experiments, readout resonator frequencies, and corresponding χ_r and κ_r rates.

APPENDIX D: CLIFFORD GROUP GENERATION

To use the cross-entropy benchmarking technique, one needs to generate arbitrary sequences of single-qubit Clifford gates. For an experimenter, the task looks like this: you need to perform an arbitrary Clifford gate in the shortest time and make as few preliminary calibration steps as possible. In our previous work [10] we describe in detail the calibration process of single-qubit rotation about the X axis at an angle of $\pi/2$ that we denote as $\sqrt{X}$ gates. Also, we keep in mind that the rotations about the Z axis can be
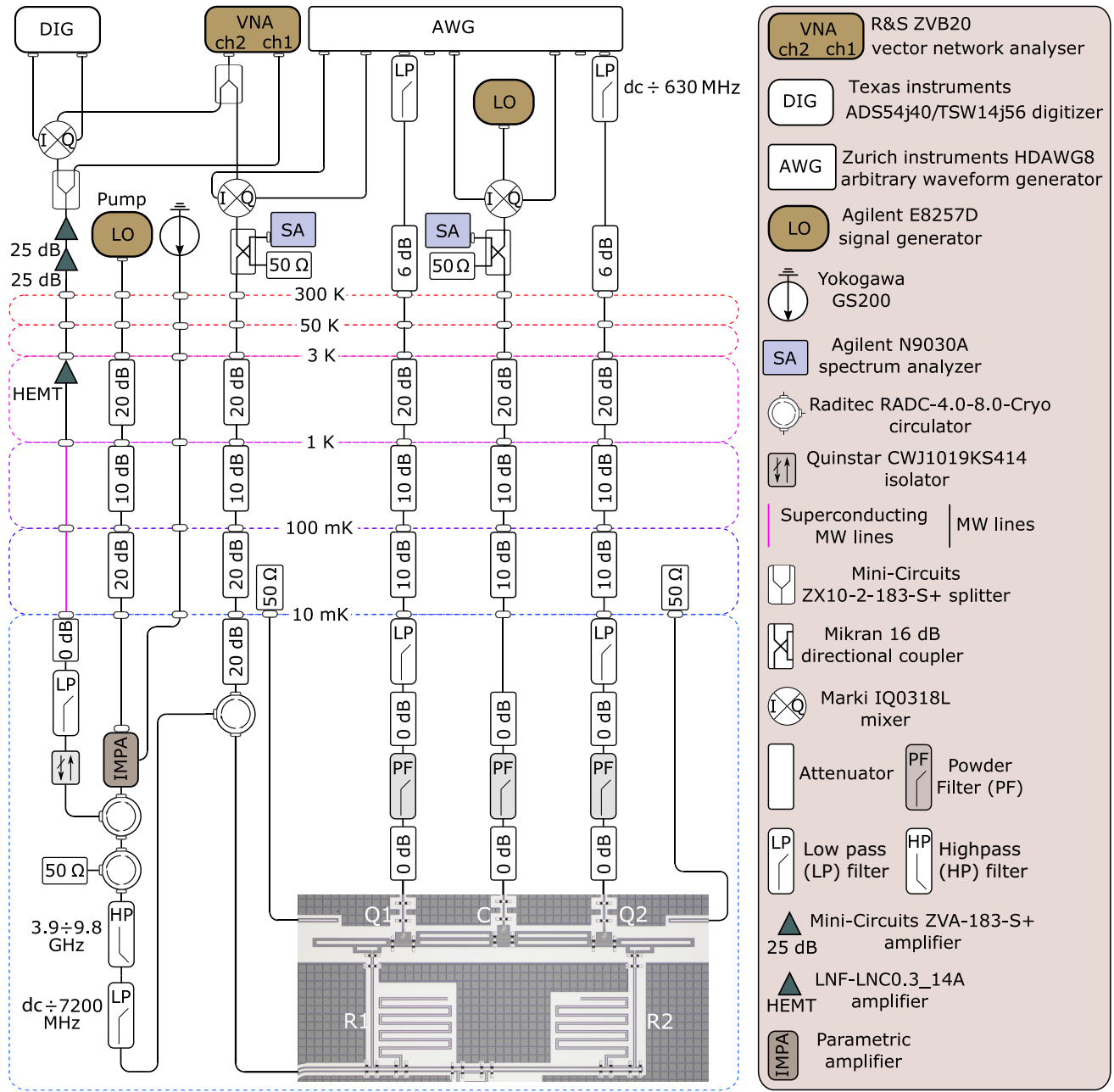
FIG. 8. Experimental setup.

virtual and cost no time. Based on this, we propose the following method. We form four sets, each of which contains 24 single-qubit gates:

$$1 : \{I, S, S^2, S^3, I, S, S^2, S^3, I, S, S^2, S^3, I, S, S^2, S^3, I, S, S^2, S^3, I, S, S^2, S^3\},$$

$$2 : \{\sqrt{X}, \sqrt{X}, \sqrt{X}, \sqrt{X}, \sqrt{X}, \sqrt{X}, \sqrt{X}, \sqrt{X}, \sqrt{X}, \sqrt{X}, \sqrt{X}, \sqrt{X}, \sqrt{X}, \sqrt{X}, \sqrt{X}, \sqrt{X}$$
$$\sqrt{X}, \sqrt{X}, \sqrt{X}, \sqrt{X}, \sqrt{X}, \sqrt{X}, \sqrt{X}, \sqrt{X}\},$$

$$3 : \{I, I, I, I, S, S, S, S, S^2, S^2, S^2, S^2, S^3, S^3, S^3, S^3, I, I, I, I, S, S, S, S\},$$

$$4 : \{I, I, I, I, I, I, I, I, I, I, I, I, I, I, I, I, \sqrt{X}, \sqrt{X}, \sqrt{X}, \sqrt{X}, \sqrt{X}, \sqrt{X}, \sqrt{X}, \sqrt{X}\}.$$

TABLE II.   Device parameters.

Parameter	Qubit 1	Qubit 2	Coupler
E_C (GHz)	0.55	0.55	0.584
E_L (GHz)	0.7507	0.7507	0.817
E_J (GHz)	1.8	1.9	2.457
f_{01} (GHz)	0.6696	0.6944	3.4098
T_1 (μs)	15.8	22.0	⋯
T_2 (μs)	4.5	5.8	⋯
$\omega_r/2\pi$ (GHz)	7.1699	7.3813	⋯
$\kappa_r/2\pi$ (MHz)	8.656	6.954	⋯
$\chi_r/2\pi$ (MHz)	0.131	0.162	⋯

Then we randomly generate an integer number i from 1 to 24 and consecutively multiply the ith gate in each set. It is easy to make sure that in this way we get 24 different Clifford operations. Moreover, gates from the first and third sets are virtual, and gates from the second and fourth sets take time not exceeding the duration of the $\sqrt{X}$ operation. Thus, implementation of an arbitrary single-qubit Clifford gate reserves a fixed time that in our case is equal to 26.6 ns.

APPENDIX E: COUPLER STATE POPULATION MEASUREMENTS

Because of the absence of an individual readout resonator for the coupling element, we need a special technique to measure the coupler population. Owing to the large interaction between the coupler and the first computational qubit, the data qubit dispersive shift conditioned by the coupler state is significant and equals 26 MHz. Hence, the drive, optimized for the coupler in the ground state, affects the qubit dynamic differently when the coupler is in the first excited state and the difference is more sufficient for the small amplitude signals.
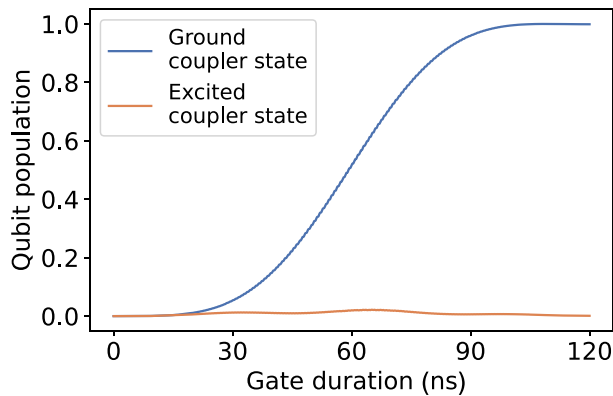

FIG. 9.   The first qubit state population dynamic under a Gaussian 120-ns π pulse for the coupler being in the ground (blue line) and the first excited (orange line) states.

The idea is as follows, as the action of the calibrated π pulse strongly depends on the coupler state, then we can use it to estimate the coupling element population. In the experiment, we choose the Gaussian π pulse with duration 120 ns (the duration of a $\pi/2$ pulse used for Clifford group generation is 13.3 ns). In Fig. 9 we show the numerical simulation of the computational qubit dynamics under this pulse when the coupler is in the ground (blue curve) and excited (orange curve) states. As one can see, such a long pulse almost preserves the qubit in the ground state for the excited coupler; meanwhile, the unexcited coupler acts as a high-fidelity X gate.

APPENDIX F: NUMERICAL ERROR ESTIMATION

We consider incoherent and coherent errors. Experimentally obtained coherence times of the computational qubits are $T_1 = 15.8$, 22.0 μs and $T_2 = 4.5$, 5.8 μs. To estimate the influence of the decoherence, we simulate the evolution of the system with the Lindblad master equation. The depolarization error of average single-qubit Clifford gates of 26-ns duration is 0.64%. The depolarization error of the 44-ns-long two-qubit CZ operation simulated under these coherence rates, assuming a noiseless coupling qubit, is 1.05%.

Because of the absence of an individual readout cavity for the coupler, the measurements of coupler coherence times were not conducted. However, as the qubits and the coupler are fluxoniums, we estimate the coupler coherence times at the flux degeneracy point $T_1 = 18$ μs and $T_2 = 5$ μs close to the data qubits' rates. The resulting depolarization error calculated by the master equation numerical solution with the noisy coupling element and ideal qubits is 0.28%. The discrepancy with experimentally obtained XEB fidelity can be attributed to a shorter coherence time of the coupler, since, unlike the computational qubits ,it is operated at the upper sweet spot.

The residual coupler population affects the fidelity of single-qubit gates implementing after the two-qubit CZ gate. We compute the residual coupler population for each computational state using Eq. (4). It equals 2.0% and 1.4% for $|01\rangle$ and $|10\rangle$ computational states. The residual coupler population of the computational states $|00\rangle$ and $|11\rangle$ is significantly smaller due to the calibration (see the right inset plot of Fig. 2). These populations significantly exceed the equilibrium thermal population of the coupler excited state of 0.07% for a 3-GHz transition frequency at 20-mK base temperature. According to the numerical estimation, if the coupler residual population is 2%, which corresponds to the maximum value after the CZ operation, the single-qubit 26-ns-long X-gate fidelity reduces down to 98.7%. The XEB technique is sensitive to such an error source. We consider the decrease of the single-qubit gate accuracy as the two-qubit coupler residual population error.

[1] Vladimir E. Manucharyan, Jens Koch, Leonid I. Glazman, and Michel H. Devoret, Fluxonium: Single Cooper-pair circuit free of charge offsets, Science **326**, 113 (2009).

[2] Long B. Nguyen, Yen-Hsiang Lin, Aaron Somoroff, Raymond Mencia, Nicholas Grabon, and Vladimir E. Manucharyan, High-coherence fluxonium qubit, Phys. Rev. X **9**, 041041 (2019).

[3] Helin Zhang, Srivatsan Chakram, Tanay Roy, Nathan Earnest, Yao Lu, Ziwen Huang, D. K. Weiss, Jens Koch, and David I. Schuster, Universal fast-flux control of a coherent, low-frequency qubit, Phys. Rev. X **11**, 011010 (2021).

[4] Il'ya Nikolaevich Moskalenko, Il'ya Stanislavovich Besedin, Ivan Andreevich Tsitsilin, Grigorii Stefanovich Mazhorin, Nikolai Nikolaevich Abramov, Aleksandr Grigor'ev, Il'ya Anatolevich Rodionov, Alina Aleksandrovna Dobronosova, Dmitrii Olegovich Moskalev, Anastasiya Aleksandrovna Pishchimova, et al., Planar architecture for studying a fluxonium qubit, JETP Lett. **110**, 574 (2019).

[5] Jens Koch, Terri M. Yu, Jay Gambetta, A. A. Houck, D. I. Schuster, J. Majer, Alexandre Blais, M. H. Devoret, S. M. Girvin, and R. J. Schoelkopf, Charge-insensitive qubit design derived from the Cooper pair box, Phys. Rev. A **76**, 042319 (2007).

[6] B. Foxen, et al., Demonstrating a continuous set of two-qubit gates for near-term quantum algorithms, Phys. Rev. Lett. **125**, 120504 (2020).

[7] Aaron Somoroff, Quentin Ficheux, Raymond A. Mencia, Haonan Xiong, Roman V. Kuzmin, and Vladimir E. Manucharyan, Millisecond coherence in a superconducting qubit, ArXiv:2103.08578 (2021).

[8] Quentin Ficheux, Long B. Nguyen, Aaron Somoroff, Haonan Xiong, Konstantin N. Nesterov, Maxim G. Vavilov, and Vladimir E. Manucharyan, Fast logic with slow qubits: Microwave-activated controlled-*Z* gate on low-frequency fluxoniums, Phys. Rev. X **11**, 021026 (2021).

[9] Feng Bao, et al., Fluxonium: An alternative qubit platform for high-fidelity operations, Phys. Rev. Lett. **129**, 010502 (2022).

[10] Ilya N. Moskalenko, Ilya A. Simakov, Nikolay N. Abramov, Alexander A. Grigorev, Dmitry O. Moskalev, Anastasiya A. Pishchimova, Nikita S. Smirnov, Evgeniy V. Zikiy, Ilya A. Rodionov, and Ilya S. Besedin, High fidelity two-qubit gates on fluxoniums using a tunable coupler, npj Quantum Inf. **8**, 130 (2022).

[11] Oleh V. Ivakhnenko, Sergey N. Shevchenko, and Franco Nori, Nonadiabatic Landau-Zener-Stückelberg-Majorana transitions, dynamics, and interference, Phys. Rep. **995**, 1 (2023).

[12] Frank Arute, Kunal Arya, Ryan Babbush, Dave Bacon, Joseph C. Bardin, Rami Barends, Rupak Biswas, Sergio Boixo, Fernando G.S.L Brandao, and David A. Buell, et al., Quantum supremacy using a programmable superconducting processor, Nature **574**, 505 (2019).

[13] Sebastian Krinner, Nathan Lacroix, Ants Remm, Agustin Di Paolo, Elie Genois, Catherine Leroux, Christoph Hellings, Stefania Lazar, Francois Swiadek, Johannes Herrmann, Graham J. Norris, Christian Kraglund Andersen, Markus Müller, Alexandre Blais, Christopher Eichler, and Andreas Wallraff, Realizing repeated quantum error correction in a distance-three surface code, Nature **605**, 669 (2022).

[14] Haonan Xiong, Quentin Ficheux, Aaron Somoroff, Long B. Nguyen, Ebru Dogan, Dario Rosenstock, Chen Wang, Konstantin N. Nesterov, Maxim G. Vavilov, and Vladimir E. Manucharyan, Arbitrary controlled-phase gate on fluxonium qubits using differential ac Stark shifts, Phys. Rev. Res. **4**, 023040 (2022).

[15] Konstantin N. Nesterov, Chen Wang, Vladimir E. Manucharyan, and Maxim G. Vavilov, Cnot gates for fluxonium qubits via selective darkening of transitions, Phys. Rev. Appl. **18**, 034063 (2022).

[16] E. Dogan, D. Rosenstock, L. L. Guevel, H. Xiong, R. A. Mencia, A. Somoroff, K. N. Nesterov, M. G. Vavilov, V. E. Manucharyan, and C. Wang, Demonstration of the two-fluxonium cross-resonance gate, ArXiv:2204.11829 (2022).

[17] Aneirin J. Baker, Gerhard B. P. Huber, Niklas J. Glaser, Federico Roy, Ivan Tsitsilin, Stefan Filipp, and Michael J. Hartmann, Single shot i-Toffoli gate in dispersively coupled superconducting qubits, Appl. Phys. Lett. **120**, 054002 (2022).

[18] I. N. Moskalenko, I. S. Besedin, I. A. Simakov, and A. V. Ustinov, Tunable coupling scheme for implementing two-qubit gates on fluxonium qubits, Appl. Phys. Lett. **119**, 194001 (2021).

[19] M. Ganzhorn, G. Salis, D. J. Egger, A. Fuhrer, M. Mergenthaler, C. Müller, P. Müller, S. Paredes, M. Pechal, and M. Werninghaus, et al., Benchmarking the noise sensitivity of different parametric two-qubit gates in a single superconducting quantum computing platform, Phys. Rev. Res. **2**, 033447 (2020).

[20] Sergio Boixo, Sergei V. Isakov, Vadim N. Smelyanskiy, Ryan Babbush, Nan Ding, Zhang Jiang, Michael J. Bremner, John M. Martinis, and Hartmut Neven, Characterizing quantum supremacy in near-term devices, Nat. Phys. **14**, 595 (2018).

[21] R. Barends, et al., Diabatic gates for frequency-tunable superconducting qubits, Phys. Rev. Lett. **123**, 210501 (2019).

[22] Eyob A. Sete, Nicolas Didier, Angela Q. Chen, Shobhan Kulshreshtha, Riccardo Manenti, and Stefano Poletto, Parametric-resonance entangling gates with a tunable coupler, Phys. Rev. Appl. **16**, 024050 (2021).